

Magnetic, thermal, and transport properties of the mixed valent vanadium oxides LuV_4O_8 and YV_4O_8

S. Das,¹ A. Niazi,¹ Y. Mudryk,² V. K. Pecharsky,³ and D. C. Johnston¹

¹Ames Laboratory and Department of Physics and Astronomy, Iowa State University, Ames, Iowa 50011

²Ames Laboratory, Iowa State University, Ames, Iowa 50011

³Ames Laboratory and Department of Materials Science and Engineering, Iowa State University, Ames, Iowa 50011

(Dated: December 5, 2018)

LV_4O_8 ($L = \text{Yb}, \text{Y}, \text{Lu}$) compounds are reported to crystallize in a structure similar to that of the orthorhombic CaFe_2O_4 structure-type, and contain four inequivalent V sites arranged in zigzag chains. We confirm the structure and report the magnetic, thermal, and transport properties of polycrystalline YV_4O_8 and LuV_4O_8 . A first-order like phase transition is observed at 50 K in both YV_4O_8 and LuV_4O_8 . The symmetry remains the same with the lattice parameters changing discontinuously. The structural transition in YV_4O_8 leads to partial dimerization of the V atoms resulting in a sudden sharp drop in the magnetic susceptibility. The V spins that do not form dimers order in a canted antiferromagnetic state. The magnetic susceptibility of LuV_4O_8 shows a sharp peak at ~ 50 K. The magnetic entropies calculated from heat capacity versus temperature measurements indicate bulk magnetic transitions below 90 K for both YV_4O_8 and LuV_4O_8 .

I. INTRODUCTION

Vanadium oxides have been of broad interest owing to their interesting properties. Binary vanadium oxides $\text{V}_n\text{O}_{2n-1}$ where $2 \leq n \leq 9$ exhibit metal to insulator and paramagnetic to antiferromagnetic transitions on cooling.¹ The only exception is V_7O_{13} which remains metallic down to 4 K.² Among ternary vanadium oxides, the normal spinel mixed valent LiV_2O_4 does not show any magnetic ordering, remains metallic down to 0.5 K and surprisingly shows heavy fermion behavior below 10 K.³ This is very different from the similar normal spinel LiTi_2O_4 which shows superconductivity below 13 K.⁴

The compound CaV_2O_4 forms in the well-known CaFe_2O_4 type structure with orthorhombic space group $Pnam$ and lattice parameters $a = 9.206 \text{ \AA}$, $b = 10.674 \text{ \AA}$, and $c = 3.009 \text{ \AA}$.^{5,6,7} The V atoms have spin $S = 1$ and form a zigzag chain system. The compound undergoes an orthorhombic to monoclinic structural distortion below 150 K and an antiferromagnetic transition at 63 K, and is an insulator.^{7,8,9} The low dimensionality of the V spin structure is very interesting since this can give rise to exotic magnetism. Indeed, there is a suggestion that a phase transition at $\simeq 200$ K in CaV_2O_4 arises from a long- to short-range chiral ordering transition with no long-range spin order either below or above this temperature.⁷ In a spin $S = 1$ zigzag chain system, depending on the ratio of the nearest-neighbor and next-nearest-neighbor interactions, there can be ground states with a Haldane gap, as well as gapless or gapped chiral ordering.¹⁰ Replacing Ca^{2+} by Na^{+1} , the same CaFe_2O_4 structure is retained but becomes metallic even below the antiferromagnetic transition at 140 K.^{11,12} Further investigations of compounds having the CaFe_2O_4 -type and related structures are clearly warranted.

The compounds LV_4O_8 ($L = \text{Yb}, \text{Y}, \text{Lu}$) have structures similar to the CaFe_2O_4 -type structure but with the modification that in LV_4O_8 , only half of the L cation

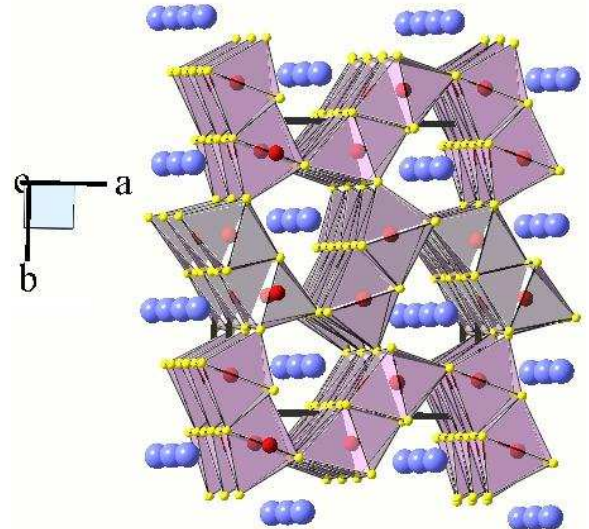


FIG. 1: (Color online) Crystal structure of the low-temperature α -phase of LV_4O_8 viewed along the c -axis. The large blue, intermediate red, and small yellow circles represent L , V and O atoms, respectively. The VO_6 octahedra share edges to form V zigzag chains running along the c -axis. The L ions occupy half of the cation sites in the CaV_2O_4 structure in an ordered fashion while the other half is vacant.

sites are occupied by L ions in an ordered manner.¹³ This results in a reduction of the unit cell symmetry from orthorhombic to monoclinic with space group $P12_1/n1$ (which is a nonisomorphic subgroup of the orthorhombic space group $Pnam$ of CaV_2O_4) and lattice parameters $a = 9.0648 \text{ \AA}$, $b = 10.6215 \text{ \AA}$, $c = 5.7607 \text{ \AA}$, and $\beta = 90.184^\circ$ for the room temperature α -phase (see below) of the Yb compound.¹³ Note that the monoclinic angle β is close to 90° and that the a -axis and b -axis lattice parameters are nearly the same as in the above orthorhombic room-temperature structure of CaV_2O_4 .

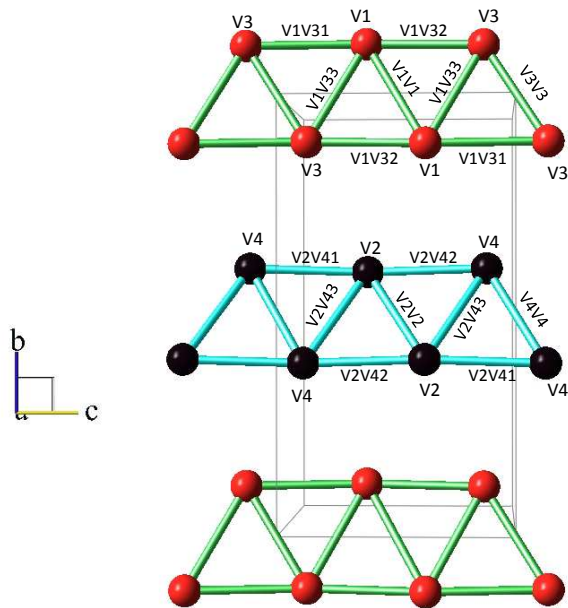


FIG. 2: (Color online) The arrangement of V atoms in the structure as viewed along the a -axis. Two distinct chains are formed by V atoms in four inequivalent sites labelled V1, V2, V3, and V4, respectively. The bond lengths between different V atoms are labelled as V1V1, V2V2, V3V3, V4V4, V1V31, V1V32, V1V33, V2V41, V2V42, and V2V43, respectively.

Figure 1 shows the structure of α - LV_4O_8 viewed along the c axis. The slightly distorted VO_6 octahedra share edges and corners to form zigzag chains along the c axis. The four V atoms in the structure occupy four inequivalent positions and form two distinct chains with two inequivalent V positions in each chain. The V-V zigzag chains as viewed along the a axis are shown in Fig. 2.

YbV_4O_8 forms in two monoclinic phases, the low temperature α -phase with space group $P12_1/n1$ and lattice parameters $a = 9.0648 \text{ \AA}$, $b = 10.6215 \text{ \AA}$, $c = 5.7607 \text{ \AA}$, and $\beta = 90.184^\circ$ and the high temperature β -phase with space group $P2_1/n11$ and lattice parameters $a = 9.0625 \text{ \AA}$, $b = 11.0086 \text{ \AA}$, $c = 5.7655 \text{ \AA}$, and $\alpha = 105.070^\circ$.¹³ The two phases differ crystallographically by the z atomic position of the Yb ions, but both contain similar zigzag chains. At 185 K the β - YbV_4O_8 undergoes a magnetic phase transition with magnetic behavior of the vanadium cations separating into Curie-Weiss and spin gap types. The magnetic transition is accompanied at the same temperature by a monoclinic to monoclinic structural phase transition arising from complete charge ordering of the V^{+3} and V^{+4} ions.¹⁴ YV_4O_8 also crystallizes in α and β forms isomorphous with α - and β - YbV_4O_8 .¹⁵ LuV_4O_8 was reported to have a homogeneity range from $LuV_4O_{7.93}$ to $LuV_4O_{8.05}$ ¹⁶ and its structure is isostructural with α - YbV_4O_8 .¹³

The structures of the above LV_4O_8 compounds are closely related to the Hollandite-type structure with either tetragonal or monoclinic crystal symmetry and chemical formula $A_xB_8O_{16}$ ($A = K, Li, Sr, Ba, Bi; B$

$= Ti, V, Mn, Ru, Rh; 1 \leq x \leq 2$).^{17,18} In the Hollandites, edge-sharing BO_6 octahedra form zigzag chains running parallel to the crystallographic c axis. The Hollandite $K_2V_8O_{16}$ undergoes a metal-insulator and a structural transition at 170 K which leads to possible dimerization of the V spins.¹⁹ The presence of a quantum phase transition from a weakly localized state to a metallic state in $BaRu_6O_{12}$ has been reported.²⁰

The magnetic susceptibilities of α - YV_4O_8 and β - YV_4O_8 show Curie-Weiss behavior in the high T region and drop sharply on cooling to temperatures between 50 and 80 K.¹⁵ For α - YV_4O_8 , the drop at 50 K appears to be a first order transition. This is different from the magnetic susceptibility of the isostructural YbV_4O_8 or similarly structured CaV_2O_4 .⁸ Curie-Weiss fits to the high T susceptibilities yielded negative Weiss temperatures indicating dominant antiferromagnetic interactions among the V spins and Curie constants much lower than expected for three V^{+3} ($S = 1$) and one V^{+4} ($S = 1/2$) spins per formula unit for both α - and β - YV_4O_8 . In order to investigate the origin of the first order-like transition in YV_4O_8 and to search for interesting magnetic ground states in these zigzag spin chain systems with modified $CaFe_2O_4$ crystallographic structure, we have synthesized polycrystalline samples of YV_4O_8 and LuV_4O_8 and report their structure, magnetic susceptibility χ , magnetization M , specific heat C , and the electrical resistivity ρ .

The remainder of the paper is organized as follows. In Sec. II, the synthesis procedure and other experimental details are reported. The structures from room temperature down to 10 K, magnetic susceptibility, magnetization, heat capacity, and electrical resistivity measurements are presented in Sec. III. We also carried out bond valence analysis to estimate the valences of the inequivalent V atoms in the mixed valent YV_4O_8 and LuV_4O_8 compounds. The results of this analysis are reported following the x-ray diffraction measurements in Sec. III. In Sec. IV, we suggest a model to explain the observed magnetic susceptibility and heat capacity behaviors of YV_4O_8 in light of the structural studies reported in Sec. III, whereas a model to explain the magnetic susceptibility and heat capacity behaviors of LuV_4O_8 is elusive. A summary of our results is given in Sec. V.

II. EXPERIMENTAL DETAILS

The samples of LV_4O_8 ($L = Y, Lu$) were prepared by solid state reaction. The starting materials for our samples were Y_2O_3 (99.995%, Alfa Aesar), Lu_2O_3 , V_2O_5 (99.999%, MV Laboratories Inc.), and V_2O_3 (99.999%, MV Laboratories Inc.). Stoichiometric amounts of L_2O_3 , V_2O_5 , and V_2O_3 were thoroughly mixed together in a glove box filled with helium gas, and pressed into pellets. The pellets were wrapped in platinum foils, sealed in evacuated quartz tubes and heated at 520 $^\circ C$ for 8–10 d. The temperature was then raised to 800 $^\circ C$ for an-

other 5–7 d. Finally the samples were heated at 1200 °C for another 7 d. The quartz tubes were then taken out of the furnace at 1200 °C and quenched in air to room temperature.

Powder x-ray diffraction measurements at room temperature were done using a Rigaku Geigerflex diffractometer with a curved graphite crystal monochromator. Temperature-dependent powder x-ray diffraction studies were done in the temperature range 10 K – 295 K using a standard Rigaku TTRAX diffractometer system equipped with a theta/theta wide-angle goniometer and a Mo $K\alpha$ radiation source.²⁹ The magnetic measurements were done using a Quantum Design superconducting quantum interference device (SQUID) magnetometer in the temperature range 1.8 K – 350 K and magnetic field range 0 – 5.5 T. The heat capacity and electrical resistivity measurements were done using a Quantum Design physical property measurement system (PPMS). For the heat capacity measurements, Apiezon N grease was used for thermal coupling between the samples and the sample platform. Heat capacity was measured in the temperature range 1.8 K – 320 K in zero, 5 T, and 9 T magnetic fields. Electrical resistivity measurements were carried out using a standard dc 4-probe technique. Platinum leads were attached to rectangular shaped pieces of sintered pellets using silver epoxy. An excitation current of 10 mA was used in the resistivity measurements in the temperature range 1.8 K – 300 K.

III. RESULTS

A. X-ray diffraction measurements

Figures 3(a) and (b) show the room temperature x-ray diffraction (XRD) patterns of powder samples of YV_4O_8 and LuV_4O_8 , respectively, along with the calculated patterns. The calculated patterns were obtained by Rietveld refinements of the observed patterns using the GSAS program suite.²¹ The refinements for both YV_4O_8 and LuV_4O_8 were done with space group $P12_1/n1$ (No. 14) (the same space group as for the low- T α -phase of YbV_4O_8) with one position for the L atom, four different positions for V atoms, and eight different positions for O atoms. All the fractional atomic positions, the lattice parameters, and the overall thermal parameter for all the atoms were varied in the refinement. The obtained best-fit lattice parameters and fractional atomic positions at 300 K are listed in Tables I and II for YV_4O_8 and LuV_4O_8 , respectively. From the refinements, small amounts (< 4 wt%) of V_2O_3 impurity phases were found in both YV_4O_8 and LuV_4O_8 samples.

Figure 4 shows the lattice parameters a , b , c , unit cell volume, and the monoclinic angle β respectively, of YV_4O_8 versus temperature. At ~ 50 K the a and b axes and the monoclinic angle α decrease sharply while the c axis and the unit cell volume increase. There is no change in the symmetry of the unit cell. The sharp change in

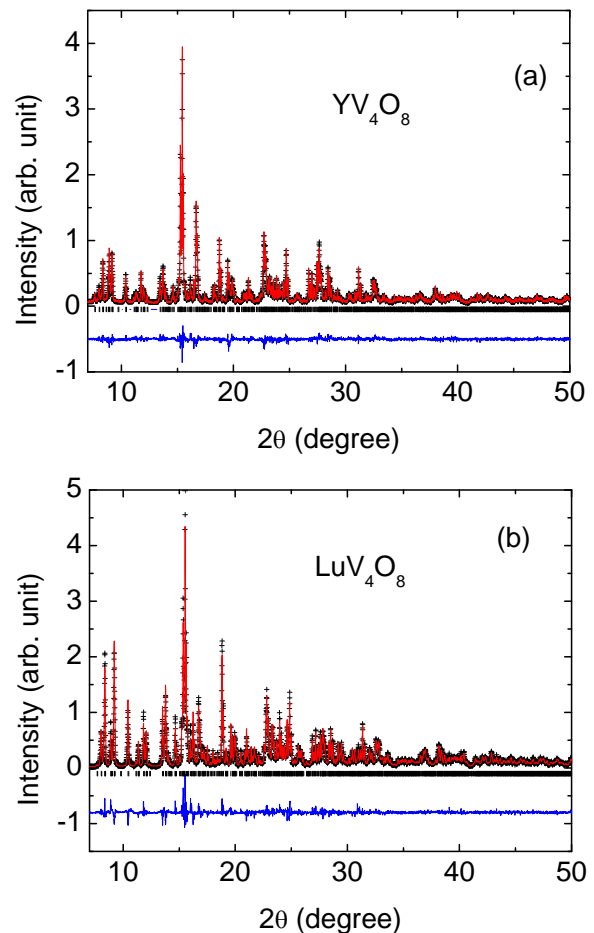


FIG. 3: (Color online) X-ray diffraction patterns of YV_4O_8 (a) and LuV_4O_8 (b), respectively, at room temperature. The solid crosses are the observed data points while the solid lines are the Rietveld fits to the data. The tick marks below the data indicate the peak positions. The solid lines below the tick marks are the difference between the observed and the calculated intensities. Small amounts (< 4 wt%) of V_2O_3 impurity phases are present in both YV_4O_8 and LuV_4O_8 samples.

the lattice parameters and the unit cell volume indicate a first order phase transition.

For LuV_4O_8 , as shown in Fig. 5, the a and b lattice parameters decrease sharply below 45 K while the c lattice parameter and the unit cell volume show a broad peak at ~ 45 K. The monoclinic angle β increases below 100 K.

Figures 6(a)-(b) and 6(c)-(d) show the V-V bond lengths versus temperature for different inequivalent V atoms in YV_4O_8 and LuV_4O_8 , respectively. For both YV_4O_8 and LuV_4O_8 , the V atoms at the four inequivalent sites form two different kinds of chains V1-V3 and V2-V4 running along the c axis as shown in Fig. 2. For the V1-V3 chain in YV_4O_8 , the V1V32 distance increases while the V1V31 distance decreases below 50 K. The other V1-V3 distances also decrease below 50 K. For LuV_4O_8 , the V2V42 distance decreases while the V2V41

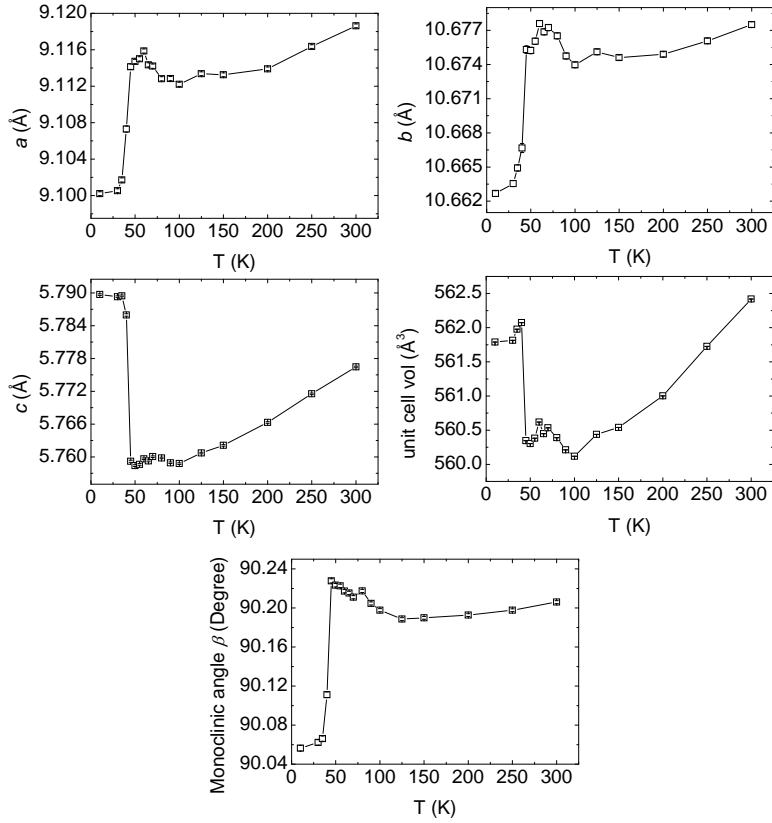


FIG. 4: Lattice parameters a , b , c , unit cell volume, and the monoclinic angle β of YV_4O_8 versus temperature T .

TABLE I: Lattice parameters and the fractional atomic positions of YV_4O_8 at 295 K, obtained by Rietveld refinement of powder XRD data. Space group: $P12_1/n1$ (No. 14); $Z = 4$ formula units/unit cell; lattice parameters: $a = 9.1186(2)$ Å, $b = 10.6775(2)$ Å, $c = 5.7764(1)$ Å, and monoclinic angle $\beta = 90.206(1)^\circ$; $R(F^2) = 0.083$. All atoms are in general Wyckoff positions $4(e)$: x , y , z . A number in parentheses gives the error in the last or last two digits of the respective quantity.

	x	y	z
Y1	0.7574(2)	0.6581(2)	0.1257(4)
V1	0.4282(3)	0.6175(3)	0.1266(8)
V2	0.4107(3)	0.0989(3)	0.1235(9)
V3	0.4537(3)	0.6111(3)	0.6263(8)
V4	0.4193(3)	0.1043(3)	0.6252(9)
O1	0.1977(9)	0.1516(1)	0.0977(21)
O2	0.1154(9)	0.4760(10)	0.1266(29)
O3	0.5278(9)	0.7744(9)	0.1285(30)
O4	0.4238(11)	0.4297(9)	0.1177(33)
O5	0.2198(9)	0.1492(10)	0.6164(22)
O6	0.1195(10)	0.4800(11)	0.6227(27)
O7	0.5119(10)	0.7934(9)	0.6155(28)
O8	0.4130(11)	0.4287(9)	0.6450(30)

TABLE II: Lattice parameters and the fractional atomic positions of LuV_4O_8 at 295 K, obtained by Rietveld refinement of powder XRD data. Space group: $P12_1/n1$ (No. 14); $Z = 4$ formula units/unit cell; lattice parameters: $a = 9.0598(2)$ Å, $b = 10.6158(2)$ Å, $c = 5.7637(1)$ Å, and monoclinic angle $\beta = 90.189(2)^\circ$; $R(F^2) = 0.095$. All atoms are in general Wyckoff positions $4(e)$: x , y , z . A number in parentheses gives the error in the last or last two digits of the respective quantity.

	x	y	z
Lu1	0.7573(2)	0.6583(1)	0.159(2)
V1	0.4269(4)	0.6170(4)	0.1281(11)
V2	0.4103(4)	0.0976(4)	0.1217(13)
V3	0.4549(4)	0.6107(4)	0.6332(11)
V4	0.4182(4)	0.1046(4)	0.6230(12)
O1	0.2019(13)	0.1609(13)	0.1091(33)
O2	0.1250(15)	0.4698(14)	0.1278(42)
O3	0.5299(14)	0.7774(14)	0.1258(45)
O4	0.4158(16)	0.4237(12)	0.1341(42)
O5	0.2098(13)	0.1670(12)	0.6358(34)
O6	0.1221(16)	0.4747(14)	0.6311(41)
O7	0.5135(14)	0.7938(14)	0.6283(42)
O8	0.4095(16)	0.4314(14)	0.6382(43)

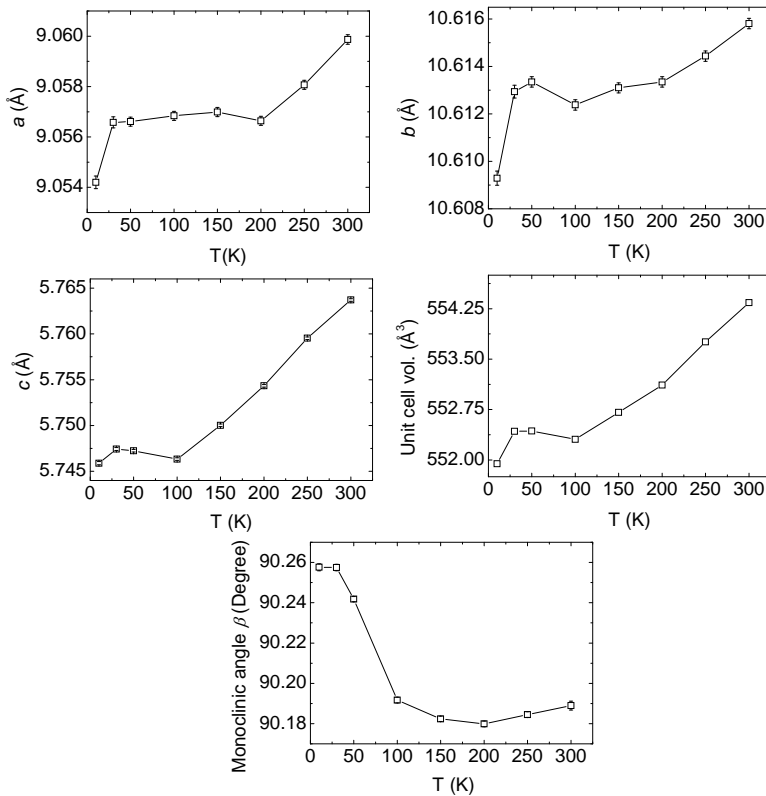


FIG. 5: Lattice parameters a , b , c , unit cell volume, and the monoclinic angle β of LuV_4O_8 versus temperature T .

distance increases below 50 K.

Bond Valence Analysis

The bond-valence method is used to calculate the valences of individual atoms in a chemical compound.²² The atomic valence of an atom is taken to be the sum of the bond valences of all bonds between that particular atom and the neighbouring atoms to which it is bonded. The bond-valence is defined as $v_i = \exp[(r_0 - r_i)/B]$ where B is fixed to the value 0.37, r_i is the interatomic distance between the particular atom and the neighbouring atom it is bonded to and r_0 is the bond-valence parameter which is obtained empirically.^{23,24} The valence for the given atom is then

$$v = \sum_i v_i = \sum_i \exp[(r_0 - r_i)/B], \quad (1)$$

where the sum is over all the nearest-neighbors to the atom of interest.

For YV_4O_8 and LuV_4O_8 , we used the bond-valence method to calculate the valences v of the different inequivalent V atoms. The V atoms are bonded only to the O atoms and the V–O interatomic distances r_i for the different V–O bonds at different temperatures were determined by the above Rietveld refinements of the structures

of the two compounds at different temperatures. The bond-valence parameters r_0 for V–O bonds are listed for $\text{V}^{3+}\text{--O}^{2-}$, $\text{V}^{4+}\text{--O}^{2-}$, and $\text{V}^{5+}\text{--O}^{2-}$ bonds in Ref. 23. We obtained an expression for $r_0(v_i)$ by fitting the three r_0 versus v_i values for V–O bonds²³ by a second order polynomial. The valences of the four inequivalent V atoms at different temperatures for YV_4O_8 and LuV_4O_8 from Eq. (1) are shown in Fig. 7.

B. Magnetic measurements

1. Magnetic susceptibility

Figure 8(a) shows the magnetic susceptibility $\chi \equiv M/H$ versus temperature T of YV_4O_8 in magnetic field $H = 100$ G. These data are in good agreement with the $\chi(T)$ of YV_4O_8 reported in Ref. 15. There is a sharp fall in the susceptibility at $T = 50$ K followed by a bifurcation in the zero-field-cooled (ZFC) and field-cooled (FC) susceptibility $\chi(T)$ below 16 K. In addition, there are two small anomalies at $T = 90$ K and $T = 78$ K. The field dependence of χ is shown in Fig. 8(b). The sharp peak at 16 K and the small anomaly at 90 K for $H = 100$ G disappear at $H = 5000$ G.

Figure 8(d) shows the ZFC and FC magnetic susceptibilities of LuV_4O_8 in $H = 100$ G. The FC susceptibility shows a sudden slope change at ~ 100 K, a broad peak

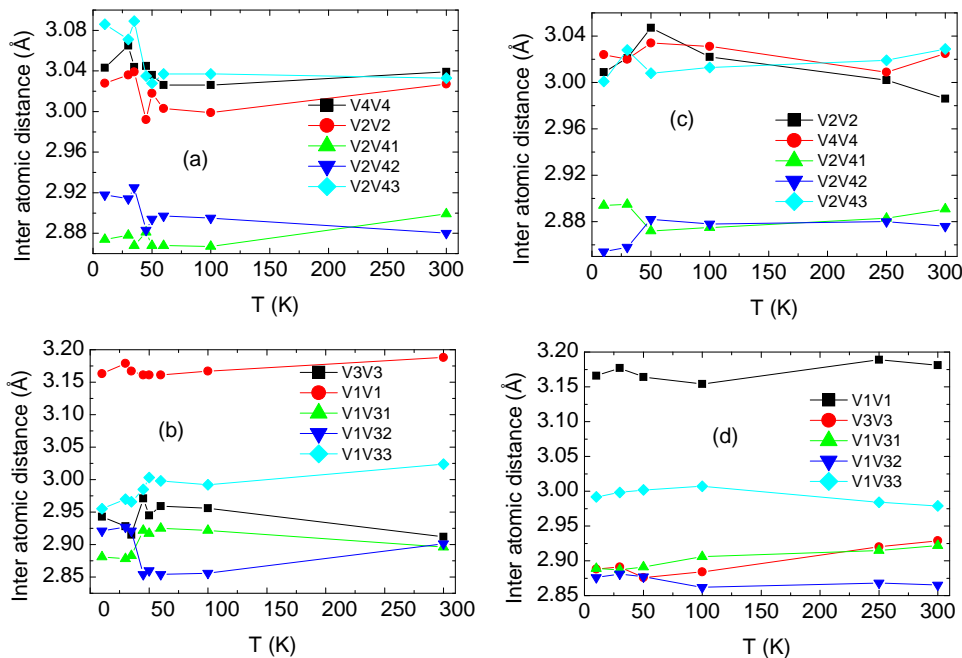


FIG. 6: (Color online) V-V bond lengths in (a)-(b) YV_4O_8 and (c)-(d) LuV_4O_8 . For the atom notations see Fig. 2.

TABLE III: Curie constant C_{Curie} , Weiss temperature θ , and temperature independent susceptibility χ_0 of YV_4O_8 and LuV_4O_8 obtained from different types of Curie-Weiss fits to the inverse susceptibility $1/\chi$ versus temperature T data in the range 200 to 300 K. The numbers in parentheses give the error in the last digit of a quantity. The parameters which do not have errors in their values were fixed during the fittings. σ^2/DOF is the goodness of fit where $\sigma^2 = \sum_i [1/\chi(T_i) - f(T_i)]^2$ and DOF (degrees of freedom) = number of data points minus the number of fit parameters. Here $\chi(T_i)$ is the measured susceptibility χ at temperature $T = T_i$ and $f(T_i)$ is the value of the fit function f at $T = T_i$.

Compound	σ^2/DOF ($10^{-1} \text{ mol}/\text{cm}^3$) ²	C_{Curie} ($\text{cm}^3 \text{ K}/\text{mol}$)	χ_0 ($10^{-4} \text{ cm}^3/\text{mol}$)	θ (K)
YV_4O_8	0.062	2.08(1)	11.8(2)	-74(1)
	0.66	2.508(2)	5.55	-105.4(3)
	1.89	2.917(5)	0	-133.0(7)
	3.67	3.375	-5.7(1)	-161.9(5)
LuV_4O_8	0.12	1.71(1)	12.9(2)	-87(1)
	1.39	2.254(2)	5.5	-136.3(4)
	3.32	2.698(4)	0	-172.4(7)
	5.96	3.375	-6.78(8)	-216.8(5)

at ~ 70 K and then a sharp peak at 49 K followed by an almost T -independent behavior below 25 K. There is a strong bifurcation in the FC and ZFC susceptibility for $T < 100$ K. The magnetic field dependence of the peak at 49 K and the small anomaly at ~ 100 K are shown in Fig. 8(e). Overall, the behavior of $\chi(T)$ of YV_4O_8 and LuV_4O_8 are distinctly different.

The high temperature $\chi(T)$ of both YV_4O_8 and LuV_4O_8 were fitted by the Curie-Weiss law

$$\chi(T) = \chi_0 + C_{\text{Curie}}/(T - \theta), \quad (2)$$

where χ_0 is the T -independent magnetic susceptibility, C_{Curie} is the Curie constant, and θ is the Weiss temper-

ature. The temperature range over which the data were fitted is $T = 200-300$ K. For YV_4O_8 , when we let all the parameters vary, we obtained $\chi_0 = 11.8 \times 10^{-4} \text{ cm}^3/\text{mol}$, $C_{\text{Curie}} = 2.08 \text{ cm}^3\text{K}/\text{mol}$, and $\theta = -74$ K. If we assume YV_4O_8 to be an insulator, then $\chi_0 = \chi_{\text{VV}} + \chi_{\text{dia}}$ where χ_{VV} is the paramagnetic Van Vleck susceptibility and χ_{dia} is the diamagnetic core susceptibility. From the standard tables,²⁵ we have for YV_4O_8 , $\chi_{\text{dia}} = -1.45 \times 10^{-4} \text{ cm}^3/\text{mol}$. The V^{3+} compound V_2O_3 has a $\chi_{\text{VV}} \sim 2 \times 10^{-4} \text{ cm}^3/\text{mol V}$.^{26,27} The V^{4+} compound VO_2 has $\chi_{\text{VV}} \sim 1 \times 10^{-4} \text{ cm}^3/\text{mol V}$.²⁸ Thus, considering that there are three moles of V^{3+} and one mole of V^{4+} ions in one mole of YV_4O_8 , we get an estimate

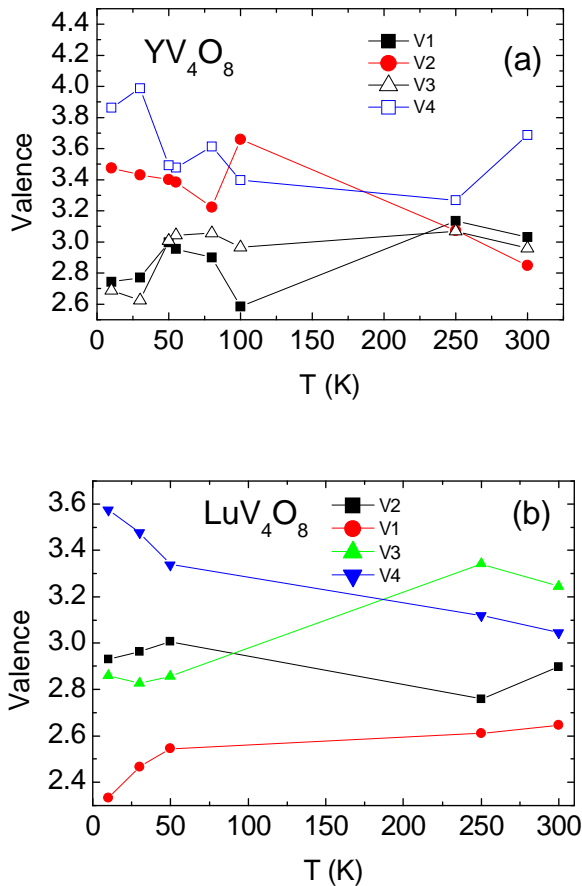


FIG. 7: (Color online) Valences of the different inequivalent V atoms versus temperature T in (a) YV_4O_8 and (b) LuV_4O_8 .

of $\chi_0 = 5.55 \times 10^{-4} \text{ cm}^3/\text{mol}$ for YV_4O_8 . For LuV_4O_8 , we have an estimate of $\chi_0 = 5.5 \times 10^{-4} \text{ cm}^3/\text{mol}$. Thus, the above value of $\chi_0 = 11.8 \times 10^{-4} \text{ cm}^3/\text{mol}$ for YV_4O_8 that we obtained by fitting the data by Eq. (2) with all the parameters varying is much too large. Keeping the value of χ_0 fixed to $5.55 \times 10^{-4} \text{ cm}^3/\text{mol}$, we obtain a $C_{\text{Curie}} = 2.476(2) \text{ cm}^3 \text{ K}/\text{mol}$ which is much less than the value $3.375 \text{ cm}^3 \text{ K}/\text{mol}$ expected for 3 V^{3+} (spin $S = 1$) and 1 V^{4+} ($S = 1/2$) atoms per formula unit with g -factor $g = 2$. Keeping χ_0 fixed to zero, we obtain a $C_{\text{Curie}} = 2.917(5) \text{ cm}^3 \text{ K}/\text{mol}$ which is closer to the expected $C_{\text{Curie}} = 3.375 \text{ cm}^3 \text{ K}/\text{mol}$. A similar analysis was done for LuV_4O_8 . Table III lists the best-fit values of the parameters C_{Curie} , χ_0 , and θ for YV_4O_8 and LuV_4O_8 obtained in these different fits. The solid lines in Figs. 8(c) and 8(f) are the Curie-Weiss fits to the $1/\chi$ data in the temperature range 200–300 K with χ_0 fixed to $5.55 \times 10^{-4} \text{ cm}^3/\text{mol}$ and $5.5 \times 10^{-4} \text{ cm}^3/\text{mol}$, respectively. As shown in Figs. 8(c) and 8(f), the observed inverse susceptibilities $1/\chi$ show stronger negative curvatures than the fits for both YV_4O_8 and LuV_4O_8 . The reason might be that the temperature range of the fits is still not high enough for the Curie-Weiss law to hold. For all the fits for each compound, we see that

θ is consistently negative indicating predominantly antiferromagnetic interactions between the V spins in both compounds.

2. Magnetization versus applied magnetic field isotherms

Figures 9(a) and (b) show the magnetization M versus applied magnetic field H isotherms at selected temperatures for LuV_4O_8 and LuV_4O_8 , respectively. The saturation magnetization M_S is obtained by fitting the high field ($1.5 \text{ T} \leq H \leq 5.5 \text{ T}$) $M(H)$ data by

$$M(H, T) = M_S(T) + \chi(T)H. \quad (3)$$

The solid lines in Figs. 9(a) and (b) are the fits of the data by Eq. (3). The fitted $M_S(T)$ for YV_4O_8 and LuV_4O_8 are shown in Fig. 9(c).

For YV_4O_8 , M_S varies rapidly with temperature below 50 K. As temperature decreases, M_S goes to a positive value of $4.13 \times 10^{-4} \mu_B/\text{F.U.}$ (F.U. means formula unit) at 50 K, where μ_B is the Bohr magneton. In view of the negative Weiss temperature found in Sec. 3 B1, this suggests a canted antiferromagnetic (AF) state. Then at 45 K, M_S decreases sharply to a negative value of $4.35 \times 10^{-4} \mu_B/\text{F.U.}$ which arises from an upward curvature to $M(H)$ which suggests the disappearance of canting and a sudden development of purely antiferromagnetic ordering. This is consistent with the observed susceptibility χ where χ was increasing with decreasing temperature but suddenly drops sharply at 49 K. As the temperature is further lowered, M_S gradually increases and finally becomes positive at 25 K and goes to a small positive value of $6.36 \times 10^{-4} \mu_B/\text{F.U.}$ at 1.8 K.

For LuV_4O_8 , the behavior of $M_S(T)$ versus T is distinctly different from that of YV_4O_8 . As temperature decreases, M_S increases sharply from zero to $3.3 \times 10^{-3} \mu_B/\text{F.U.}$ at 45 K in what appears to be a first-order transition. The data suggest the development of a canted AF state below 50 K, where the canting continuously goes to zero by 20 K, which can also be observed in the susceptibility data in Fig. 8(d) where χ increases sharply at 49 K. Then, as the temperature is further lowered, M_S starts decreasing, becoming negative at 25 K and then remaining almost constant down to 1.8 K.

Figures 10(a)–(d) and 10(e)–(h) show the $M(H)$ loops at different temperatures for YV_4O_8 and LuV_4O_8 , respectively. For YV_4O_8 , measurable hysteresis is observed below 16 K. At 1.8 K, the remanent magnetization is $0.0007 \mu_B/\text{F.U.}$ and the coercive field is 400 G. For LuV_4O_8 , on the other hand, hysteresis is observed only around the transition at 50 K. At 45 K, the magnetization loop shows a remanent magnetization of $0.003 \mu_B/\text{F.U.}$ and a coercive field of 1050 G. As we move away from the transition at 50 K, the hysteresis disappears.

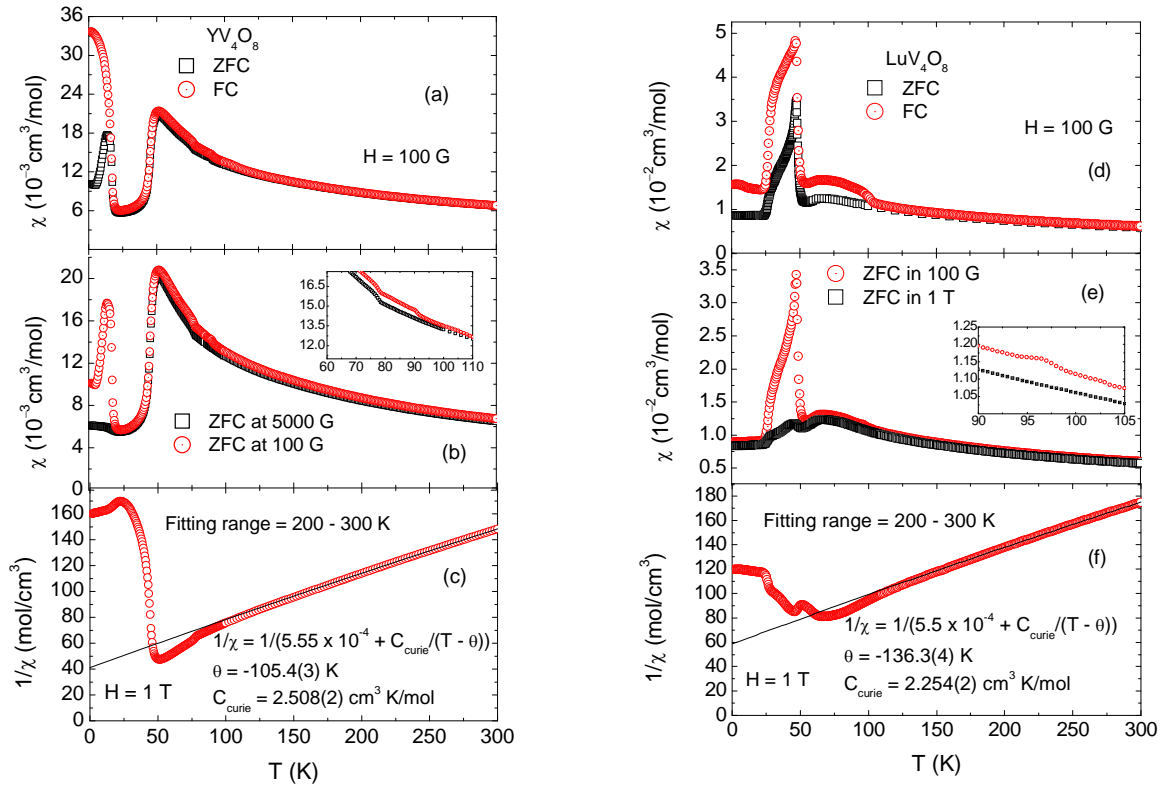


FIG. 8: (Color online) Zero-field-cooled (ZFC) and field-cooled (FC) magnetic susceptibility (a) YV_4O_8 and (d) LuV_4O_8 . (b) ZFC $\chi(T)$ in 5000 G and 100 G fields of YV_4O_8 and (e) ZFC χ in 100 G and 1 T fields of LuV_4O_8 . The insets in (b) and (e) show the anomalies in χ at 90 K and 78 K for YV_4O_8 and at 96 K for LuV_4O_8 , respectively. The inverse susceptibilities $1/\chi$ versus T in 1 T of YV_4O_8 and LuV_4O_8 are shown in (c) and (f), respectively, where the solid lines are Curie-Weiss fits to the data in the temperature range 200 – 300 K.

C. Heat capacity measurements

Figure 11(a) shows the molar heat capacity C versus temperature T of YV_4O_8 in zero and 9 T magnetic fields. $C(T)$ shows a sharp peak at $T = 77$ K and two small anomalies at $T = 81$ K (pointed by the arrow) and $T = 45$ K. There is a small magnetic field dependence of $C(T)$ at 45 K as shown in the inset of Fig. 11(a).

The magnetic contribution to the heat capacity $C_{\text{mag}}(T)$ was obtained by $C_{\text{mag}}(T) = C(T) - C_{\text{latt}}(T)$ where the lattice heat capacity $C_{\text{latt}}(T)$ is estimated from the Debye model

$$C_{\text{latt}}(T) = 9xnN_Ak_B \left(\frac{T}{\theta_D}\right)^3 \int_0^{\theta_D/T} \frac{y^4 e^y}{(e^y - 1)^2} dy, \quad (4)$$

where n is the number of atoms per formula unit, N_A is Avagadro's number, k_B is Boltzman's constant, θ_D is the Debye temperature, and x is a scaling factor which we had to introduce to get a considerable overlap of Eq. (4) with the measured C at high T . Plots of C_{latt} versus T were obtained for various values of the Debye temperature θ_D and x , and were compared to the plot of measured $C(T)$ versus T . The $C_{\text{latt}}(T)$ with the maximum

overlap with the plot of $C(T)$ data at high temperatures was chosen.

For YV_4O_8 , we obtained the best fit of $C_{\text{latt}}(T)$ by Eq. (4) with $\theta_D = 600$ K and $x = 0.96$ for $T > 200$ K. Figure 11(b) shows the plot of $C_{\text{latt}}(T)$ along with the measured $C(T)$ for YV_4O_8 . Figure 11(c) shows the magnetic contribution to the heat capacity $C_{\text{mag}}(T)/T \equiv [C(T) - C_{\text{latt}}(T)]/T$ for YV_4O_8 and Fig. 11(d) shows the magnetic entropy $S_{\text{mag}}(T)$ versus T of YV_4O_8 given by

$$S_{\text{mag}}(T) = \int_0^T \frac{C_{\text{mag}}(T)}{T} dT. \quad (5)$$

The change in S_{mag} over the temperature range 0 K to 90 K in which the magnetic transitions occur is 32.5 J/mol K. If the V spins order, then the magnetic entropy associated with the spin ordering S_{spin} is given by

$$S_{\text{spin}} = \sum_i n_i R \ln(2S_i + 1), \quad (6)$$

where the sum is over V spins S_i in a formula unit, n_i is the number of spins S_i , and R is the molar gas constant. Using $n_i = 3 \text{ V}^{+3}$ ($S = 1$) and 1 V^{+4} ($S = 1/2$) per formula unit gives $S_{\text{mag}} = 33.14$ J/mol K which is very close

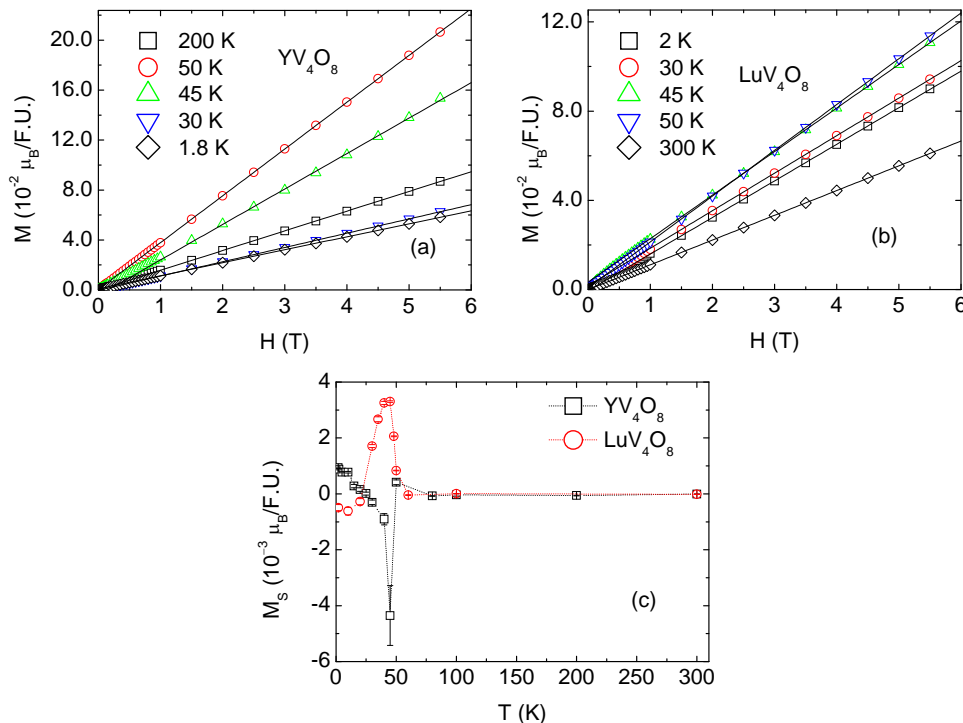


FIG. 9: (Color online) Magnetization M versus magnetic field H at different temperatures of (a) YV_4O_8 and (b) LuV_4O_8 . The solid lines are the fits of the high field ($1.5 \text{ T} \leq H \leq 5.5 \text{ T}$) $M(H)$ data by Eq. (3). The values of the saturation magnetization M_S versus T obtained from the fits are shown in (c).

(within 2%) to the value of S_{mag} obtained above. This indicates that our estimation of $C_{\text{latt}}(T)$ is reasonable.

Figure 12(a) shows the $C(T)$ of LuV_4O_8 in zero and 9 T magnetic fields. There is a peak at $T = 80 \text{ K}$ and two small kinks at 62 K and 48 K, pointed out by two arrows, respectively. The magnetic field dependence of $C(T)$ is negligible. Figure 12(b) shows the zero field $C(T)$ and the $C_{\text{latt}}(T)$ for LuV_4O_8 from Eq. (4). For LuV_4O_8 , the values $\theta_D = 600 \text{ K}$ and $x = 0.96$ produced the $C_{\text{latt}}(T)$ with the maximum overlap with $C(T)$ at high $T > 150 \text{ K}$. Figure 12(c) shows $C_{\text{mag}}(T)/T$ versus T for LuV_4O_8 . The two kinks pointed out by the arrows in Fig. 12(a) can be seen prominently here. The magnetic entropy S_{mag} calculated from Eq. (5) versus T is shown in Fig. 12(d). The total magnetic entropy change up to 150 K is 34.0 J/mol K, which again agrees very well with the above value of 33.1 J/mol K for disordered V spins. A sharp peak occurs in $C_{\text{mag}}(T)$ at $\approx 80 \text{ K}$ with two additional kinks highlighted by two vertical arrows at 45 K and $\approx 60 \text{ K}$, respectively, as shown in Fig. 12(c).

D. Electrical resistivity measurements

Figures 13(a) and (b) show the electrical resistivity ρ versus temperature T measured on pieces of sintered pellets of LuV_4O_8 and YV_4O_8 , respectively. On the scale of the figures, the resistivities are nearly temperature-independent above 50 K and 60 K, respectively, and

strongly increase below those temperatures, suggesting the occurrence of metal to insulator transitions upon cooling below those temperatures. The insets in Figs. 13(a) and (b) show the respective $\log_{10}(\rho)$ versus T for the two compounds. For both compounds, $\log_{10}(\rho)$ increases with decreasing T showing apparent semiconducting behaviors over the whole T range. However, the nearly T -independent behaviors at the highest temperatures suggest metallic behavior as just noted. Polycrystalline pellets of metallic oxides are notorious for showing semiconducting-like behavior due to insulating material in the grain boundaries. A plot of $\ln(\rho)$ versus $1/T$ for LuV_4O_8 is shown in Fig. 13(c). We fitted these data by

$$\rho = \rho_0 \exp[\Delta/k_B T], \quad (7)$$

where Δ is the activation energy, ρ_0 is a constant, and k_B is Boltzmann's constant. The solid line in Fig. 13(c) is the fit in the T range 55 K ($1/T = 0.018 \text{ K}^{-1}$) to 75 K ($1/T = 0.0133 \text{ K}^{-1}$) where the $\ln[\rho(1/T)]$ data are approximately linear. The obtained fit parameters are $\rho_0 = 7.44(3) \Omega \text{ cm}$ and $\Delta = 84.6(1) \text{ meV}$.

IV. DISCUSSION

Tables IV and V list the temperatures at which anomalies were observed in the $\chi(T)$, $C(T)$, and $\rho(T)$ measurements of YV_4O_8 and LuV_4O_8 , respectively. Upon cool-

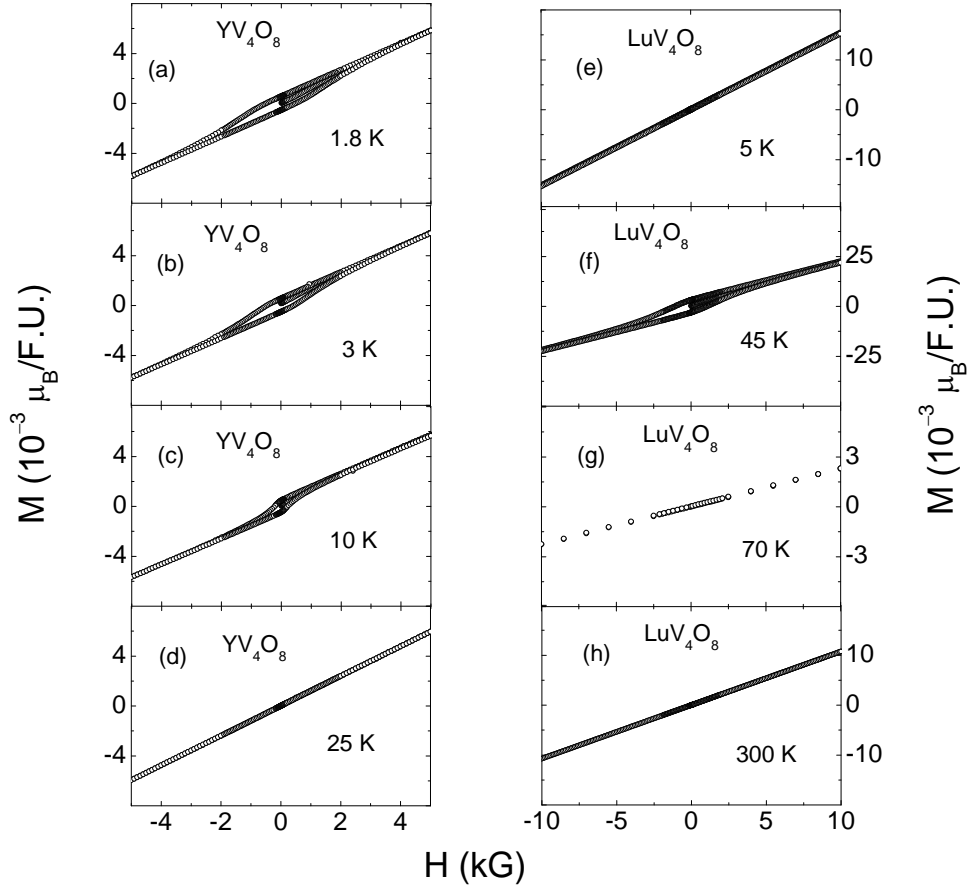


FIG. 10: Magnetization M versus magnetic field H loops at different temperatures of YV_4O_8 and LuV_4O_8 .

TABLE IV: Different temperatures at which anomalies were observed in $\chi(T)$, $C(T)$, and $\rho(T)$, respectively, for YV_4O_8 .

	χ	C	ρ
T_1	16		
T_2	50	45	
T_3			60
T_4	78	77	
T_5		81	
T_6	90		

ing below ≈ 50 K, a sharp decrease of the V1V31 distance, increase of the V1V32 distance, and an increase in the other V1-V3 distances as shown in Fig. 6(b) suggest dimerization of the V1 and V3 spins in the V1-V3 chain (see Fig. 2) in YV_4O_8 . The valences of V1 and V3 from Fig. 7(a) are close to 3 suggesting that both have spin $S = 1$. From the Curie-Weiss fit of the magnetic susceptibility in Fig. 8(c), the dominant interactions between the V spins are antiferromagnetic. We infer that the dimerization leads to a suppression of the magnetic susceptibility in the V1-V3 chain below 50 K. For the other V2-V4 chain, below 50 K, all the V-V interatomic

TABLE V: Different temperatures at which anomalies were observed in $\chi(T)$, $C(T)$, and $\rho(T)$, respectively, for LuV_4O_8 .

	χ	C	ρ
T_1	25		
T_2	50	48	50
T_3		62	
T_4		80	
T_5	100		

distances increase as shown in Fig. 6(a), allowing the spins to order antiferromagnetically. The calculated valences of the V2 and V4 atoms in Fig. 7(a) point towards a decrease in the spin states of those V atoms. Both effects probably contribute to the sudden sharp drop in the magnetic susceptibility below 50 K in Figs. 8(a) and (b).

The transition observed in $\chi(T)$ at 50 K in Figs. 8(a) and (b) for YV_4O_8 also appears in $C_{\text{mag}}(T)$ and $\rho(T)$ for this compound at a similar temperature in Figs. 11(a), (c), and Fig. 13(b). The presence of the anomaly in $C(T)$ strengthens our interpretation of dimerization due to structural transition and long range antiferromagnetic

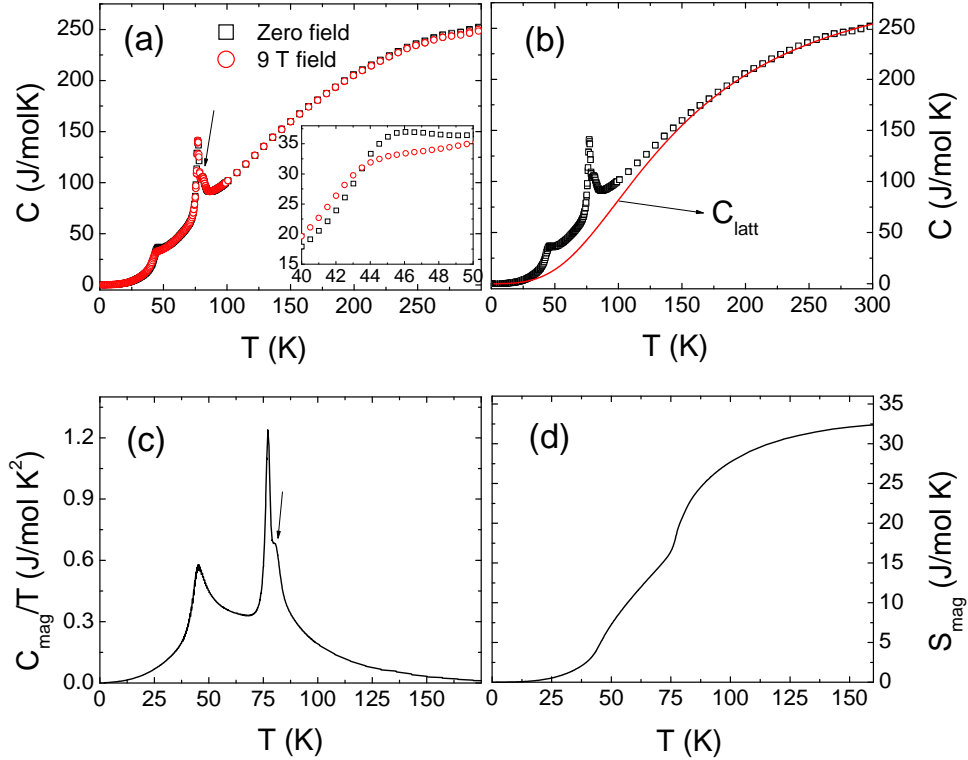


FIG. 11: (Color online) (a) Heat capacity C versus temperature T of YV_4O_8 in 0 and 9 T magnetic fields. The arrow points to a tiny anomaly at 81 K. The inset shows a small magnetic field dependence of the heat capacity anomaly at 45 K. (b) The $C(T)$ in zero field from (a) along with the $C_{\text{latt}}(T)$ obtained using Eq. (4) with $x = 0.96$ and $\theta_D = 600$ K. (c) $C_{\text{mag}}(T)/T$ versus T . The arrow points to the tiny anomaly at 81 K also seen in Fig. 11(a). (d) Magnetic entropy $S_{\text{mag}}(T)$ obtained from Eq. (5).

ordering at 50 K. However, there is no anomaly in C_{mag} at 16 K where the ZFC-FC $\chi(T)$ data in Fig. 8(a) show a strong bifurcation which disappears at high fields as shown in Fig. 8(b). No change in $C_{\text{mag}}(T)$ in Fig. 11(c) is observed at 16 K, suggesting that the bifurcation of the ZFC-FC $\chi(T)$ may be due to weak canting of the antiferromagnetically ordered V spins. The presence of magnetic hysteresis with a very small ($0.0007 \mu_B/\text{F.U.}$) remnant magnetization at 2 K shown in Fig. 10(a) and a small almost T -independent $M_S(T)$ below 16 K shown in Fig. 9(c) are all consistent with the occurrence of canted antiferromagnetism below 16 K. There are two additional anomalies at 75 K and 90 K which appear in both $\chi(T)$ and $C_{\text{mag}}(T)$, the origins of which are unclear.

The dimerization of the V spins in one of the chains and formation of spin singlets in YV_4O_8 is very similar to the spin-Peierls transition observed in CuGeO_3 at 14 K.³⁰ The occurrence of a metal to insulator transition at 60 K (which is very close to the temperature of the spin singlet formation) as shown in Fig. 13(b) suggests that YV_4O_8 is a rare example where a metal to spin singlet insulator transition takes place. Such a Peierls-like transition has been observed in the tetragonal rutile VO_2 at 340 K^{31,32} and in the spinel MgTi_2O_4 at 260 K.^{33,34} In both VO_2 and MgTi_2O_4 , a complete structural transition occurs at the temperature of the metal to spin

singlet transition,^{33,35} unlike YV_4O_8 , where only the lattice parameters change without a lowering of the crystal symmetry.

For LuV_4O_8 , the magnetic susceptibility in Figs. 8(d) and (e) shows no evidence of formation of spin singlets. There is no anomaly in $C_{\text{mag}}(T)$ in Fig. 12(c) at ≈ 100 K at which a slope change occurs in $\chi(T)$ in Fig. 8(d). On the other hand, a sharp peak occurs in $C_{\text{mag}}(T)$ at ≈ 80 K, where no anomaly in $\chi(T)$ occurs. This might indicate the onset of short-range ordering at ≈ 100 K followed by long-range ordering at ≈ 80 K. From Figs. 8(d) and (e), the $\chi(T)$ shows a sharp increase at ≈ 50 K, whereas in Fig. 12(c) there is only a small kink in $C_{\text{mag}}(T)$ at this T . The absence of a sharp anomaly in C_{mag} at 50 K might indicate the development of a canted AF state at that temperature.

The Curie-Weiss fits to the high T χ for both YV_4O_8 and YV_4O_8 yield Curie constants that are considerably lower than expected, which leads to the possibility of both these compounds being metallic.

V. SUMMARY

We have synthesized powder samples of YV_4O_8 and LuV_4O_8 whose crystallographic structure consists of two

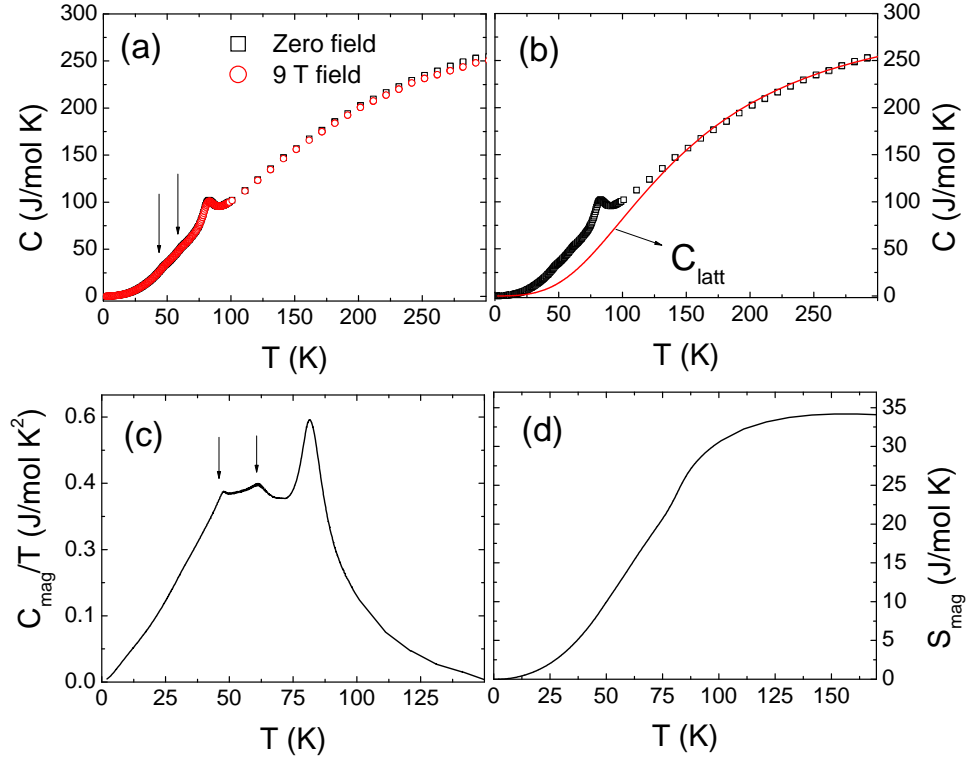


FIG. 12: (Color online) (a) Heat capacity C versus temperature T of LuV_4O_8 in 0 and 9 T magnetic fields. The arrows point to two kinks at 62 K and 48 K, respectively. (b) The heat capacity $C(T)$ from (a) in zero field along with the $C_{\text{latt}}(T)$ obtained from Eq. (4) with $x = 0.96$ and $\theta_D = 600$ K. (c) $C_{\text{mag}}(T)/T$ versus T . The arrows point to the kinks at 62 K and 48 K also seen in Fig. 12(a). (d) Magnetic entropy $S_{\text{mag}}(T)$ obtained from Eq. (5).

distinct one-dimensional zigzag chains running along the crystallographic c -axis. X-ray diffraction measurements down to 10 K reveal a first-order-like phase transition with a sudden change in the lattice parameters and unit cell volume at 50 K in YV_4O_8 . However, the high and low temperature structures could be refined using the same space group indicating no lowering of the symmetry of the unit cell due to the structural transition. As a result of the transition, one of the chains dimerizes. The magnetic susceptibility of YV_4O_8 exhibits a sharp first-order-like decrease at 50 K followed by a bifurcation in the ZFC-FC susceptibility below 16 K. The anomaly at 50 K is suggested to arise from the dimerization of the $S = 1$ chain and antiferromagnetic (AF) ordering of the other chain. The AF ordered spins then become canted below 16 K. The change in the magnetic entropy calculated from heat capacity measurements also agrees very well with ordering of three $S = 1$ and one $S = 1/2$ disordered spins per formula unit. The lattice parameters of LuV_4O_8 exhibit a small anomaly at ~ 50 K but not as sharp as in YV_4O_8 . The magnetic susceptibility of LuV_4O_8 shows a broad peak at ~ 60 K followed by a sharp first-order-

like increase at 50 K. The 50 K anomaly is suppressed at higher fields. For both compounds, Curie-Weiss fits to the high T susceptibilities yield Curie constants which are much lower than expected. Electrical resistivity measurements on sintered pellets indicate metal to insulator-like transition at 60 K and 50 K for YV_4O_8 and LuV_4O_8 , respectively. It would be very interesting to study single crystals of these compounds. Single crystal resistivity measurements are needed to determine if these materials are metallic or not at high temperatures. Measurements such as NMR or neutron scattering that would provide microscopic information about the spin dynamics would also be valuable to clarify the nature of the magnetic ordering transitions in YV_4O_8 and LuV_4O_8 .

Acknowledgments

Work at the Ames Laboratory was supported by the Department of Energy-Basic Energy Sciences under Contract No. DE-AC02-07CH11358.

¹ U. Schwingenschlöggl and V. Eyert, Ann. Phys. (Leipzig) **13**, 475 (2004).

² S. Kachi, K. Kosuge, and H. Okinaka, J. Solid State Chem.

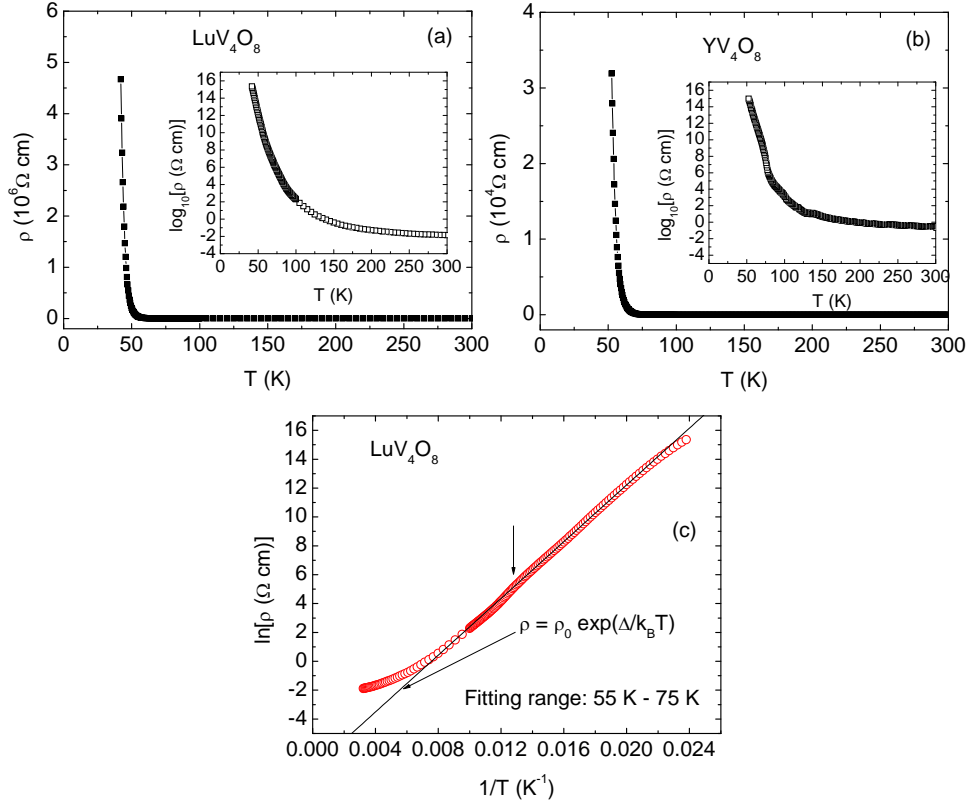


FIG. 13: Electrical resistivity ρ versus temperature T measured on sintered pellets of (a) LuV_4O_8 and (b) YV_4O_8 . Insets in (a) and (b) show $\log(\rho)$ versus T for LuV_4O_8 and YV_4O_8 , respectively. (c) $\ln(\rho)$ versus $1/T$ for LuV_4O_8 . The solid line in (c) is the fit to the data by Eq. (7) in the temperature range 55 K ($1/T = 0.018 \text{ K}^{-1}$) to 75 K ($1/T = 0.0133 \text{ K}^{-1}$) where the data are approximately linear.

- 6, 258 (1973).
- ³ S. Kondo, D. C. Johnston, C. A. Swenson, F. Borsa, A. V. Mahajan, L. L. Miller, T. Gu, A. I. Goldman, M. B. Maple, D. A. Gajewski, E. J. Freeman, N. R. Dilley, R. P. Dickey, J. Merrin, K. Kojima, G. M. Luke, Y. J. Uemura, O. Chmaissem, and J. D. Jorgensen, *Phys. Rev. Lett.* **78**, 3729 (1997).
- ⁴ D. C. Johnston, *J. Low Temp. Phys.* **255**, 145 (1976).
- ⁵ B. F. Decker and J. S. Kasper, *Acta Crystallogr.* **10**, 332(1957).
- ⁶ J. M. Hastings, L. M. Corliss, W. Kunnmann, and S. La Placa, *J. Phys. Chem. Solids* **28**, 1089(1967).
- ⁷ A. Niazi, S. L. Bud'ko, D. L. Schlagel, J. Q. Yan, T. A. Lograsso, A. Kreyssig, S. Das, S. Nandi, A. I. Goldman, A. Honecker, R. W. McCallum, M. Reehuis, O. Pieper, B. Lake, and D. C. Johnston, *Phys. Rev. B* **79**, 104432 (2009).
- ⁸ X. Zong, B. J. Suh, A. Niazi, J. Q. Yan, D. L. Schlagel, T. A. Lograsso, and D. C. Johnston, *Phys. Rev. B* **77**, 014412 (2008).
- ⁹ O. Pieper, B. Lake, A. Daoud-Aladine, M. Reehuis, K. Prokes, B. Klemke, K. Kiefer, J. Q. Yan, A. Niazi, D. C. Johnston, and A. Honecker, *Phys. Rev. B* **79**, 180409(R) (2009).
- ¹⁰ T. Hikihara, M. Kaburagi, H. Kawamura, and T. Tonegawa, *J. Phys. Soc. Jpn.* **69**, 259 (2000).
- ¹¹ K. Yamaura, M. Arai, A. Sato, A. B. Karki, D. P. Young, R. Movshovich, S. Okamoto, D. Mandrus, and E. Takayama-Muromachi, *Phys. Rev. Lett.* **99**, 196601 (2007).
- ¹² H. Sakurai, *Phys. Rev. B* **78**, 094410 (2008).
- ¹³ Y. Kanke and K. Kato, *Chem. Mater.* **9**, 141 (1997).
- ¹⁴ K. Friese, Y. Kanke, A. N. Fitch, and A. Grzechnik, *Chem. Mater.* **19**, 4882 (2007).
- ¹⁵ M. Onoda, *Acta. Cryst.* **B59**, 429 (2003).
- ¹⁶ K. Kitayama, *Bull. Chem. Soc. Jpn.* **51**, 1358 (1978).
- ¹⁷ A. Byström and A. M. Byström, *Acta Cryst.* **3**, 146 (1950).
- ¹⁸ C. C. Torardi, *Mater. Res. Bull.* **20**, 705 (1985).
- ¹⁹ M. Isobe, S. Koishi, N. Kouno, J.-I. Yamaura, T. Yamauchi, H. Ueda, H. Gotou, T. Yagi, and Y. Ueda, *J. Phys. Soc. Jpn.* **75**, 073801 (2006).
- ²⁰ Z. Q. Mao, T. He, M. M. Rosario, K. D. Nelson, D. Okuno, B. Ueland, I. G. Deac, P. Schiffer, Y. Liu, and R. J. Cava, *Phys. Rev. Lett.* **90**, 186601 (2003).
- ²¹ A. C. Larson and R. B. Von Dreele, "General Structure Analysis System (GSAS)", Los Alamos National Laboratory Report LAUR 86-748 (2000); B. H. Toby, *J. Appl. Cryst.* **34**, 210 (2001).
- ²² I. D. Brown and R. D. Shannon, *Acta Cryst. Sect. A* **29**, 266 (1973).
- ²³ I. D. Brown and D. Altermatt, *Acta Cryst.* **B41**, 244 (1985).
- ²⁴ N. E. Brese and M. O'Keeffe, *Acta Cryst.* **B47**, 192 (1991).
- ²⁵ R. D. Shannon, *Acta Crystallogr.* **A32**, 751 (1976).
- ²⁶ E. D. Jones, *Phys. Rev.* **137**, A978 (1965).
- ²⁷ M. Takigawa, E. T. Ahrens, and Y. Ueda, *Phys. Rev. Lett.* **76**, 283 (1996).

- ²⁸ J. P. Pouget, D. S. Schreiber, H. Launois, D. Wohlleben, A. Casalot, and G. Villeneuve, *J. Phys. Chem. Solids* **33**, 1961 (1972).
- ²⁹ A. P. Holm, V. K. Pecharsky, K. A. Gschneidner, Jr., R. Rink, and M. Jirmanus, *Rev. Sci. Instrum.* **75**, 1081 (2004).
- ³⁰ M. Hase, I. Terasaki, and K. Uchinokura, *Phys. Rev. Lett.* **70**, 3651 (1993).
- ³¹ F. J. Morin, *Phys. Rev. Lett.* **3**, 34 (1959).
- ³² J. P. Pouget, H. Launois, T. M. Rice, P. Dernier, A. Gos-
sard, G. Villeneuve, and P. Hagenmuller, *Phys. Rev. B* **10**,
1801 (1974).
- ³³ M. Isobe and Y. Ueda, *J. Phys. Soc. Jpn.* **71**, 1848 (2002).
- ³⁴ J. Zhou, G. Li, J. L. Luo, Y. C. Ma, Dan Wu, B. P. Zhu,
Z. Tang, J. Shi, and N. L. Wang, *Phys. Rev. B* **74**, 245102
(2006).
- ³⁵ J. B. Goodenough, *J. Solid State Chem.* **3**, 490 (1971).